Journal of Alloys and Compounds 522 (2012) 51–62

Contents lists available at SciVerse ScienceDirect

Journal of Alloys and Compounds

journal homepage: www.elsevier.com/locate/jallcom

A novel thermal decomposition approach for the synthesis of silica-iron oxide core–shell nanoparticles

P.N.R. Kishore, P. Jeevanandam*

Department of Chemistry, Indian Institute of Technology Roorkee, Roorkee 247667, Uttarakhand, India

ARTICLE INFO

Article history:
Received 17 October 2011
Received in revised form 5 January 2012
Accepted 15 January 2012
Available online 28 January 2012

Keywords:
Thermal decomposition
Core–shell nanoparticles
Iron oxide nanoparticles
Superparamagnetism
Photocatalyst

ABSTRACT

A simple thermal decomposition approach for the synthesis of magnetic nanoparticles consisting of silica as core and iron oxide nanoparticles as shell has been reported. The iron oxide nanoparticles were deposited on the silica spheres (mean diameter = 244 ± 13 nm) by the thermal decomposition of iron (III) acetylacetonate, in diphenyl ether, in the presence of SiO_2. The core–shell nanoparticles were characterized by X-ray diffraction, infrared spectroscopy, field emission-scanning electron microscopy coupled with energy dispersive X-ray analysis, transmission electron microscopy, diffuse reflectance spectroscopy, and magnetic measurements. The results confirm the presence of iron oxide nanoparticles on the silica core. The core–shell nanoparticles are superparamagnetic at room temperature indicating the presence of iron oxide nanoparticles on silica. The core–shell nanoparticles have been demonstrated as good photocatalyst for the degradation of Rhodamine B.

1. Introduction

Magnetic core–shell nanoparticles are of immense interest in recent times due to their applications in waste water treatment, immobilization of biomolecules, immunological assays, surface-enhanced Raman scattering, etc. [1–4]. There are different types of magnetic core–shell particles reported such as polymer [5,6], protein [7], silver coated Fe_3O_4 [8], and silica [9–11]. Amongst the different core–shell nanoparticles, magnetic silica microspheres with silica as core and iron oxide nanoparticles as shell are well known for their applications in catalysis, bio-separation, drug delivery, genomic DNA isolation, and environmental remediation [9–14]. They have been widely used as humidity sensors [15] and catalysts for growing carbon nanotubes [16]. Silica spheres are also known for their biocompatibility and stability against chemical degradation [17–19].

The reported synthetic methods for the preparation of magnetic silica core–shell nanoparticles include layer-by-layer assembly [17], sonochemical deposition [20], electrostatic adsorption [21], ferrite plating [22], aerosol assisted synthesis [23], hydrothermal chemical-vapour deposition [24], sol–gel [25], phase transfer [26], micro-contact printing [27], spin coating [28], micro-emulsion route [29], and bio-polymer template method [30]. There are a number of disadvantages associated with the existing synthetic methods. For example, a separate coupling agent should be used in the case of layer-by-layer assembly [17]. In ferrite plating and electrostatic adsorption methods, desorption of magnetic particles from the surface of silica takes place when the pH is increased during the synthesis. In the case of sonochemical deposition, the precursor ($Fe(CO)_5$) may get thermally decomposed if the temperature of the sonication bath exceeds −50 °C [20]. Aerosol pyrolysis is relatively expensive and some methods take longer time (15 h to 10 days) for the deposition.

In the present study, a simple thermal decomposition approach has been reported for the synthesis of silica-iron oxide core–shell nanoparticles. The deposition of iron oxide nanoparticles on silica was made by a single step thermal decomposition of iron (III) acetylacetonate, in diphenyl ether, in the presence of silica spheres. The core–shell nanoparticles were expected to exhibit interesting magnetic properties which can lead to useful applications.

Iron oxide nanoparticles have been known for their catalytic activity against the photo degradation of organic dyes which cause air and water pollution [31]. The rate of degradation of the dyes is usually slow, in sunlight, in the absence of a catalyst. Various nanoparticles (α-Fe_2O_3, Al_2O_3, ZnO, etc.) have been used as catalysts for the degradation of dyes in aqueous solution [32–34]. Rhodamine B (RhB) is one of the cationic dyes which are not bio-degradable in water [32]. In the present study, the photocatalytic activity of the synthesized core–shell nanoparticles has been demonstrated using the photodegradation of RhB in aqueous solution.

* Corresponding author. Tel.: +91 1332 285444; fax: +91 1332 286202.
E-mail address: jeevafcy@iitr.ernet.in (P. Jeevanandam).

0925-8388/$ – see front matter © 2012 Elsevier B.V. All rights reserved.
doi:10.1016/j.jallcom.2012.01.076

Table 1
Experimental details and the nomenclature of the synthesized silica-iron oxide core–shell nanoparticles.

Sl. no.	Iron (III) acetylacetonate (mmol)	Silica type and amount used	Name	Crystallite size of iron oxide (nm) (calcined at 750 °C)
1	0.5	Activated, 1 mmol	SF-1	12.0
2	1	Activated, 1 mmol	SF-2	16.1
3	1	Unactivated, 1 mmol	SF-3	–

2. Experimental

2.1. Reagents

Tetraethyl orthosilicate (98%, ACROS®), ethanol (99.9%), ammonia solution (25%), iron (III) acetylacetonate (>99%, ACROS®), diphenyl ether (98%), and methanol (99%) were used as received.

2.2. Synthesis

The preparation of silica-iron oxide core–shell nanoparticles involves two steps as discussed below in detail.

2.2.1. Preparation of silica microspheres

Silica spheres were prepared by the Stöber process [35]. About 3.7 ml of tetraethyl orthosilicate was added drop wise to a solution containing 88.0 ml of ethanol and 12.0 ml of ammonia in a 250 ml beaker under vigorous stirring. The resultant mixture was kept for constant gentle stirring for about 24 h at room temperature. The white precipitate obtained was centrifuged and washed with ethanol. The as-prepared silica was then calcined at 500 °C for 3 h inside a muffle furnace (Nabertherm, heating rate = 2 °C/min). The calcination step activates the silica thus increasing the available active sites for the subsequent deposition of iron oxide nanoparticles [36,37].

2.2.2. Deposition of iron oxide nanoparticles on silica spheres

Iron oxide nanoparticles were deposited on the silica spheres by the thermal decomposition of iron (III) acetylacetonate in diphenyl ether [38]. The synthetic details are given in Table 1 and the procedure is as follows.

About 0.17 g (0.5 mmol) or 0.35 g (1 mmol) of iron (III) acetylacetonate and 0.06 g (1 mmol) of silica were added to 10 ml of diphenyl ether in a round bottom flask. The contents were refluxed in air at about 225 °C for 70 min. The slurries obtained were cooled to room temperature. Then, about 30 ml of methanol was added and the obtained precipitates were centrifuged at 2500 rpm for about 20 min. The precipitates were washed with methanol and dried at about 90 °C overnight. Dark brown coloured powders were obtained (yield = 85–100 mg) which were then calcined in air at two different temperatures, 350 °C and 750 °C for 3 h inside a muffle furnace. Calcination at 350 °C led to a reddish brown powder whilst calcination at 750 °C led to a powder with intense reddish colour. Unactivated silica was also used for the deposition of iron oxide nanoparticles to understand the effect of activation of silica on the deposition of iron oxide nanoparticles. The nomenclature of the prepared silica-iron oxide core–shell nanoparticles is also given in Table 1.

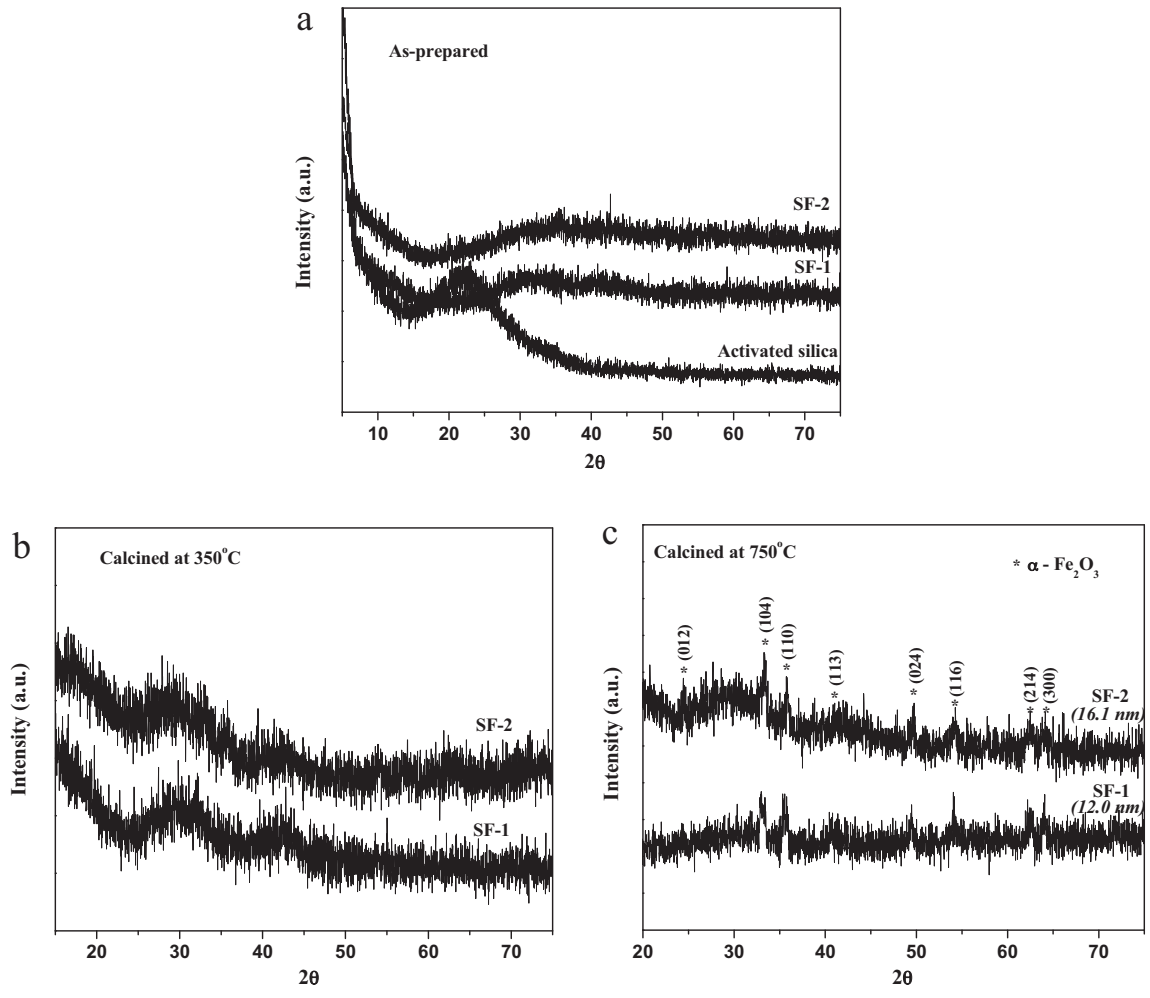

Fig. 1. XRD patterns of (a) pure activated silica, as-prepared SF-1 and SF-2, (b) after calcination at 350 °C and (c) after calcination at 750 °C.

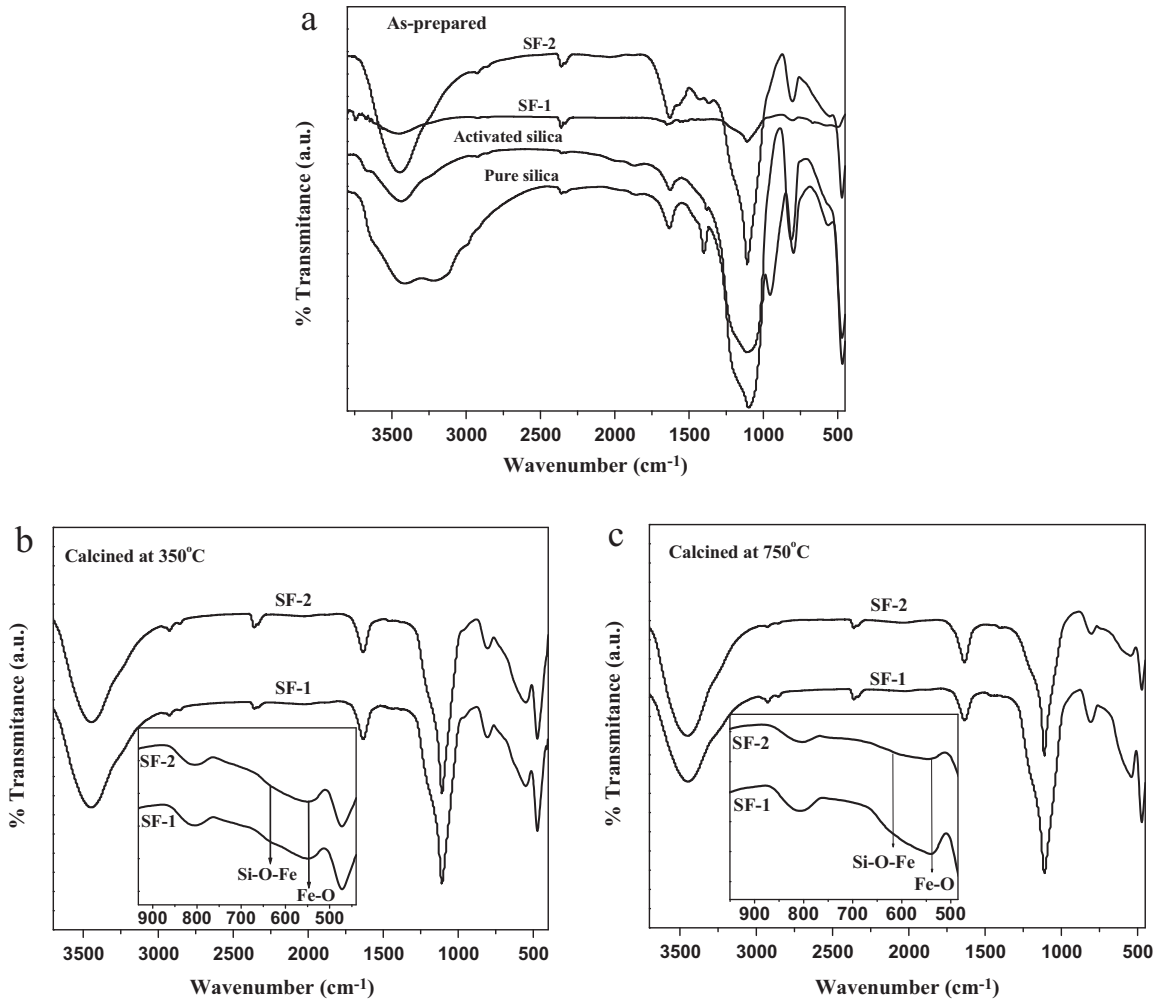

Fig. 2. FT-IR spectra of silica-iron oxide core–shell nanoparticles: (a) as-prepared, (b) after calcination at 350 °C and (c) after calcination at 750 °C.

2.3. Photocatalytic activity studies

The photodegradation of RhB in aqueous solution was used as the test reaction [32]. To about 3 ml of 0.02 mmol Rhodamine B aqueous solution in a quartz cuvette (path length = 10 mm, volume = 3 mL), 10 mg of the catalyst (silica-iron oxide core–shell nanoparticles) was added and sonicated for 10 min to achieve complete dispersion of the catalyst. Then, 0.225 ml of 30% H_2O_2 solution was added and the mixture was irradiated under UV light (λ = 365 nm) at room temperature for about 2 h. The photodegradation of the dye was monitored by recording UV–visible spectra as a function of time.

2.4. Characterization

All the samples were characterized using XRD, FT-IR, UV–Visible spectroscopy, FE-SEM coupled with EDX analysis, Zeta potential measurements, transmission electron microscopy, diffuse reflectance spectroscopy and SQUID measurements. Powder XRD patterns were recorded on a Brucker AXS D8 diffractometer operating with Cu Kα radiation (λ = 1.5406 Å) with a scan speed of 2°/min. A Thermo Nicolet Nexus Fourier transform infrared (FT-IR) spectrometer was used for recording the IR spectra using KBr pellet method. Zeta potential measurements were carried out on a Malvern Zetasizer (Nanoseries, Model: Nano – ZS90). For the Zeta potential measurements, about 0.1 mg each of the sample powder was dispersed in about 1 ml of Millipore water® and the measurements were made on the suspensions. The morphology of the samples were analysed using a FEI Quanta 200F microscope operating at 20 kV coupled with an energy dispersive X-ray analysis (EDXA) facility.

TEM analysis was done on a Philips CM 200 microscope operating at 200 kV. Carbon or lacey carbon coated copper grids were employed for the TEM studies. Diffuse reflectance spectra were recorded on a Shimadzu UV-3600 UV-Visible-NIR spectrophotometer using a diffuse reflectance accessory in the wavelength region 300–800 nm using $BaSO_4$ as the reference. Magnetic measurements (M–H) were done on a Quantum Design (MPMSXL) magnetometer by varying the field up to 70 kOe at 300 K and 5 K. Zero field cooled (ZFC) and field cooled (FC) measurements were carried out using the same instrument with temperature varying from 300 K to 5 K at an applied field of 1000 Oe. For recording the UV–visible spectra of Rhodamine B, during the photodegradation studies, a Shimadzu UV-1800 spectrophotometer was used.

3. Results and discussion

3.1. XRD analysis

The XRD patterns of pure activated silica along with the core–shell nanoparticles before and after calcination are shown

Table 2
IR band positions and their assignments for the silica-iron oxide core–shell nanoparticles.

Band position (cm^{-1})						Assignment
SF-1 as-prepared	SF-1 calcined at 350 °C	SF-1 calcined at 750 °C	SF-2 as-prepared	SF-2 calcined at 350 °C	SF-2 calcined at 750 °C	
1104	1106	1112	1104	1106	1112	(Si—O—Si) asym. stretch
803	810	814	803	810	814	(Si—O—Si) sym. stretch
485	472	472	466	472	472	δ(Si—O—Si)
–	552	550	–	552	550	ν(Fe—O)

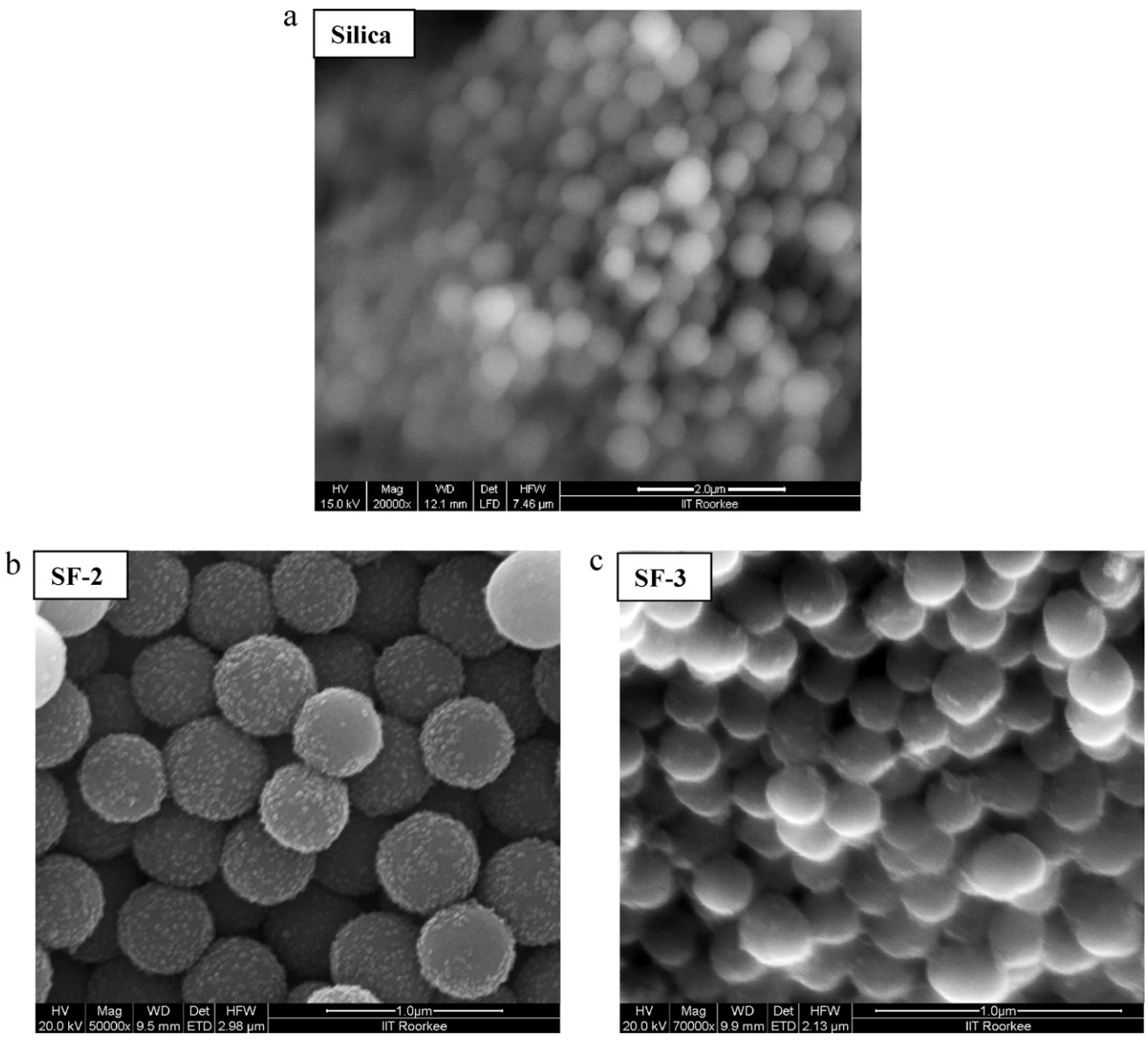

Fig. 3. SEM images of (a) silica, (b) SF-2 after calcination at 350 °C and (c) SF-3 after calcination at 350 °C.

in Fig. 1. Pure silica is amorphous. The core–shell nanoparticles (SF-1 and SF-2) before and after calcination at 350 °C show no peaks due to any of the iron oxide phases (Fig. 1(a) and (b)). This is attributed to the presence of ultrafine iron oxide nanoparticles on the silica spheres. The XRD patterns of the silica-iron oxide core–shell nanoparticles (SF-1 and SF-2), after calcination at 750 °C, show peaks due to α-Fe_2O_3 (JCPDS file no. 86-0550). The crystallite size of α-Fe_2O_3 was calculated using Debye–Scherrer's formula and the crystallite size varies from ∼12 nm to ∼16 nm depending on the concentration of iron (III) acetylacetonate (Table 1).

3.2. FT-IR analysis

The IR spectra of pure silica, activated silica and silica-iron oxide core–shell nanoparticles (SF-1 and SF-2) before and after calcination are shown in Fig. 2. The bands near 3500 cm^{-1} and 1600 cm^{-1} are attributed to O—H stretching and bending, respectively which arise from the surface hydroxyl groups of silica (Si—OH) [39]. There is evidence for the presence of organic impurities and the absence of H-bonding in the case of activated silica. In the IR spectrum of unactivated silica (Fig. 2a), the broad band near about 3220 cm^{-1} indicates the presence of H-bonding in between the surface hydroxyl groups [40,41]. The bands near 1396, 947 and 561 cm^{-1} arise from organic impurities and are attributed to C—H bending, C—H rocking and tetramer of tetraethyl orthosilicate, respectively [42]. These bands disappear in the case of activated silica indicating the absence of organic impurities after the calcination. The other observed bands in the range of 1500–400 cm^{-1}

Table 3
Zeta potential measurements on different silica samples.

Sl. no.	Sample	Zeta potential (mV)
1	Unactivated silica	−38.1
2	Fe $(C_5H_7O_2)_3$ incubated on unactivated silica	−28.4
3	Activated silica	−28.4
4	Fe $(C_5H_7O_2)_3$ incubated on activated silica	−1.3

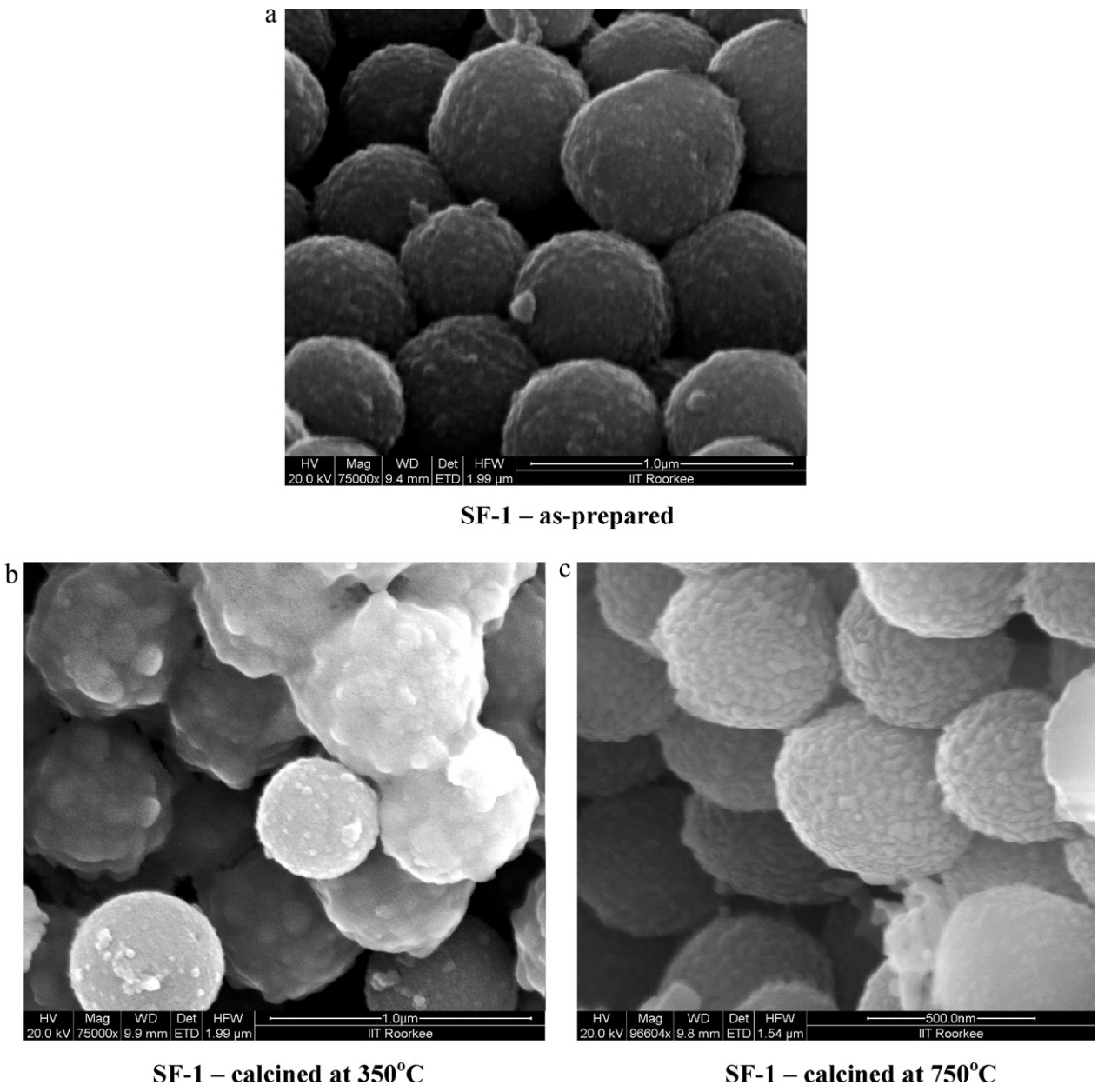

Fig. 4. SEM images of SF-1: (a) as-prepared, (b) after calcination at 350 °C and (c) after calcination at 750 °C.

Table 4
EDX results of (i) SF-1 and (ii) SF-2 (before and after calcination). The analysis was done on five different spots.

Before calcination				Calcined at 350 °C				Calcined at 750 °C			
% C	% O	% Si	% Fe	% C	% O	% Si	% Fe	% C	% O	% Si	% Fe
(i) SF-1											
16.0	37.8	37.3	8.9	10.4	25.1	40.8	23.7	4.2	16.8	55.5	23.5
18.4	41.2	33.8	6.6	11.3	28.5	39.2	21.1	2.1	17.3	59.4	21.2
19.9	35.8	35.1	9.2	7.2	28.8	43.8	20.3	0.0	18.7	56.1	25.1
24.3	37.8	30.8	7.2	11.7	31.3	37.9	19.0	0.0	13.9	61.0	25.1
(ii) SF-2											
27.8	34.9	33.5	8.6	6.0	26.8	55.7	11.5	13.7	33.4	47.6	5.2
24.9	31.9	38.7	7.2	7.9	21.8	58.4	11.8	12.7	33.2	49.0	5.1
24.3	33.5	38.0	6.0	17.4	37.9	36.8	7.9	5.5	12.8	65.3	16.4
13.6	11.6	60.1	7.9	18.7	38.8	35.1	7.4	6.4	16.3	61.4	15.8
30.3	13.6	45.8	17.4	8.6	31.9	50.7	8.8	10.8	22.1	52.4	14.7

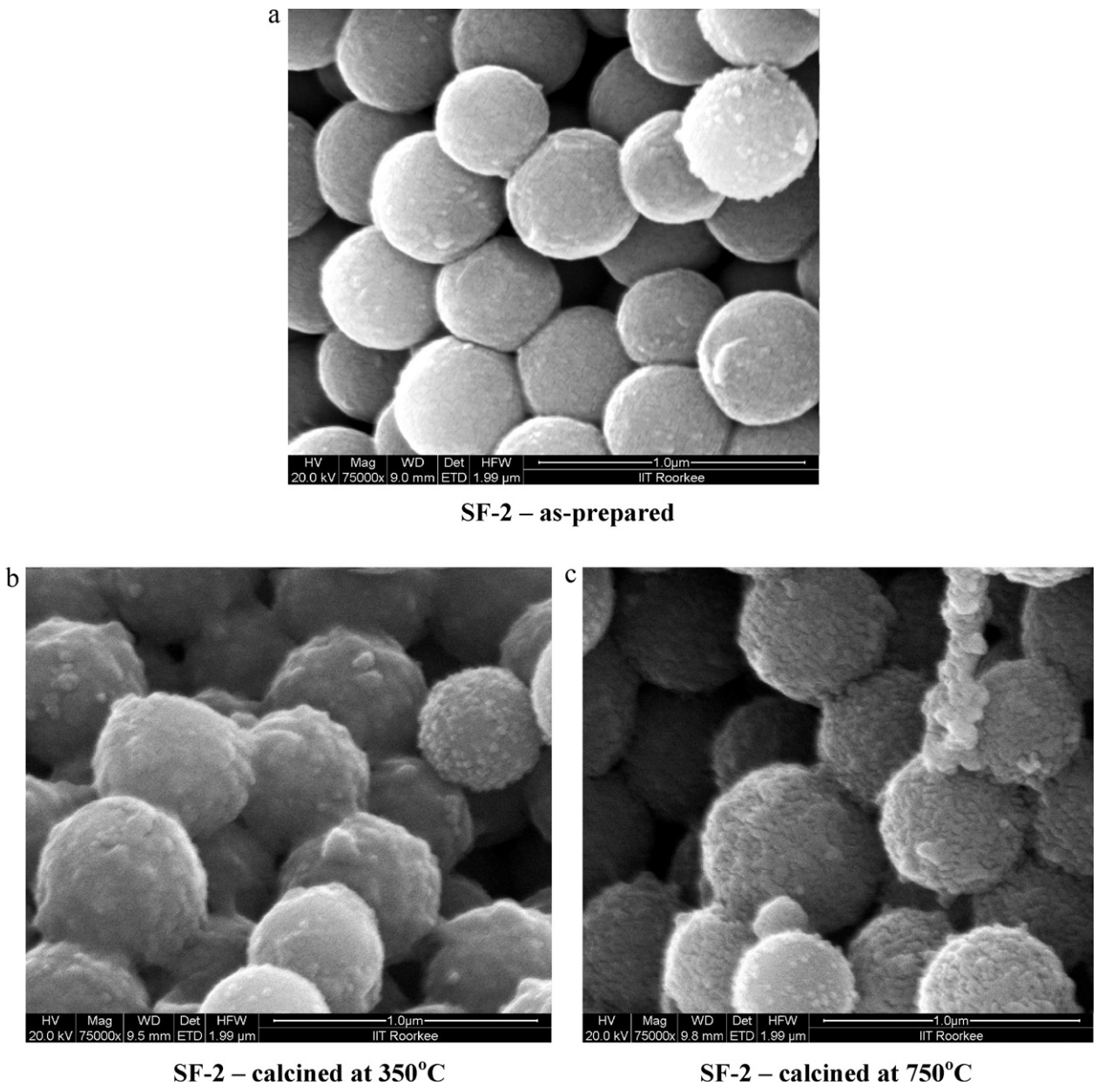

Fig. 5. SEM images of SF-2: (a) as-prepared, (b) after calcination at 350 °C and (c) after calcination at 750 °C.

along with their assignments are given in Table 2. All the magnetic microsphere samples (SF-1 and SF-2) show bands at about 1110 cm^{-1}, 800 cm^{-1} and 472 cm^{-1} which are attributed to, respectively asymmetric stretching, symmetric stretching and bending modes of Si—O—Si group [43]. The calcined samples show bands near 552 cm^{-1} which is attributed to the characteristic Fe—O stretch in iron oxide nanoparticles [44]. The presence of a shoulder observed near 645 cm^{-1} for the calcined samples (insets of Fig. 2(b) and (c)) is attributed to Si—O—Fe bond [43].

3.3. Zeta potential measurements

Zeta potential measurements were carried out on unactivated silica, activated silica, and after incubating the silica (both unactivated and activated) with $Fe(acac)_3$. The measured Zeta potential values are summarized in Table 3.

In general, silica is negatively charged and the surface charge of silica comes from the dissociation of silanol groups as shown in the following equation.

$$Si{-}OH_2^{\oplus} \overset{\overset{\oplus}{H}}{\longleftrightarrow} Si{-}OH \overset{\overset{\oplus}{H}}{\longleftrightarrow} Si{-}O^{\ominus} \quad (1)$$

The surface charge decreases as the number of surface hydroxyl groups decreases. The surface charge on the unactivated silica decreases from −38.1 mV to −28.4 mV after incubating with iron (III) acetylacetonate. The decrease in the Zeta potential is attributed to the anchoring of iron (III) acetylacetonate molecules with the surface hydroxyl groups. A large reduction in the surface charge is observed after incubating the iron complex on the activated silica (from −28.4 mV to −1.3 mV). This is attributed to the fact that better anchoring of iron (III) acetylacetonate occurs on activated silica.

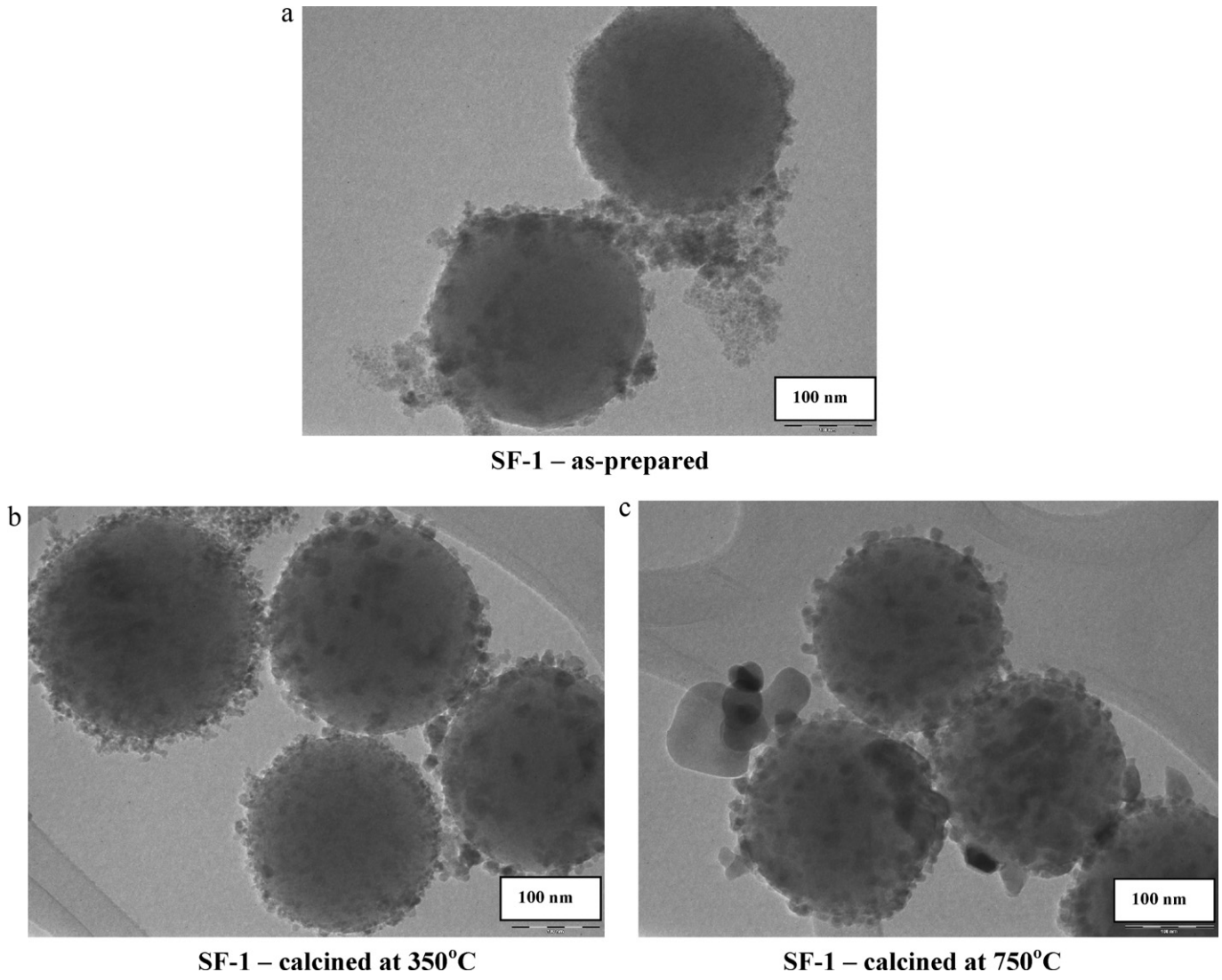

Fig. 6. TEM images of SF-1: (a) as-prepared, (b) after calcination at 350 °C and (c) after calcination at 750 °C.

3.4. FE-SEM/EDX analysis

The SEM images of silica and silica-iron oxide core–shell particles, prepared using activated as well as unactivated silica (SF-2 and SF-3, respectively), are shown in Fig. 3. It can be seen that the deposition of iron oxide nanoparticles is better when activated silica spheres are used (Fig. 3(b) versus Fig. 3(c)). Hence for further studies, activated silica spheres were used for the deposition of iron oxide nanoparticles. The effect of calcination temperature on the core–shell particles (SF-1 and SF-2) is shown in Figs. 4 and 5. In all the cases, with increase in calcination temperature, the growth of iron oxide particles can be noticed.

The weight percentages of different elements present in the silica-iron oxide core–shell nanoparticles (SF-1 and SF-2), as analysed by EDX, are given in Table 4(i) and (ii). The EDX analyses indicate the presence of Si, O and Fe in all the core–shell nanoparticles. The weight percent of iron on unactivated silica microspheres was lower (3.2–8.8%). In SF-1, the percentage of iron varies from 6.6 to 9.2. On calcination at 350 °C, the iron percentage increases to 19.0–23.7% and to 19.7–25.1% on further calcination at 750 °C. The carbon content decreases with an increase in the calcination temperature. Sample SF-2, before calcination, has a relatively non-uniform presence of iron (6.0–17.4%). On calcination at 350 °C, the percentage of iron varies from 7.4 to 11.8 and it varies from 5.1 to 16.4% after calcination at 750 °C. It can be concluded based on EDXA that a relatively uniform deposition of iron oxide nanoparticles on silica spheres is observed in sample SF-1, i.e. when lower concentration of iron (III) acetylacetonate (0.5 mmol) was employed during the thermal decomposition.

3.5. TEM studies

The TEM images for the silica-iron oxide core–shell nanoparticles (SF-1) are shown in Fig. 6. The presence of iron oxide nanoparticles on silica spheres can be clearly seen. The iron oxide particle size histograms for the calcined samples (Fig. 7) indicate that the mean size of iron oxide nanoparticles is 7.1 ± 0.7 nm after calcination at 350 °C. It increases to 13.9 ± 1.4 nm after calcination at 750 °C, which is comparable to the crystallite size calculated from the XRD analysis (12 nm).

3.6. Diffuse reflectance spectral studies

The diffuse reflectance spectra of the silica-iron oxide core–shell nanoparticles (SF-1 and SF-2) are shown in Fig. 8. In general, iron oxides show bands due to single electron transition ($^6A_1 \rightarrow {}^4T_2$) in the range of 650–710 nm [45]. Also, an electron pair transition (EPT) ($^6A_1 + {}^6A_1 \rightarrow {}^4T_1 + {}^4T_1$) is observed for all the iron oxides in

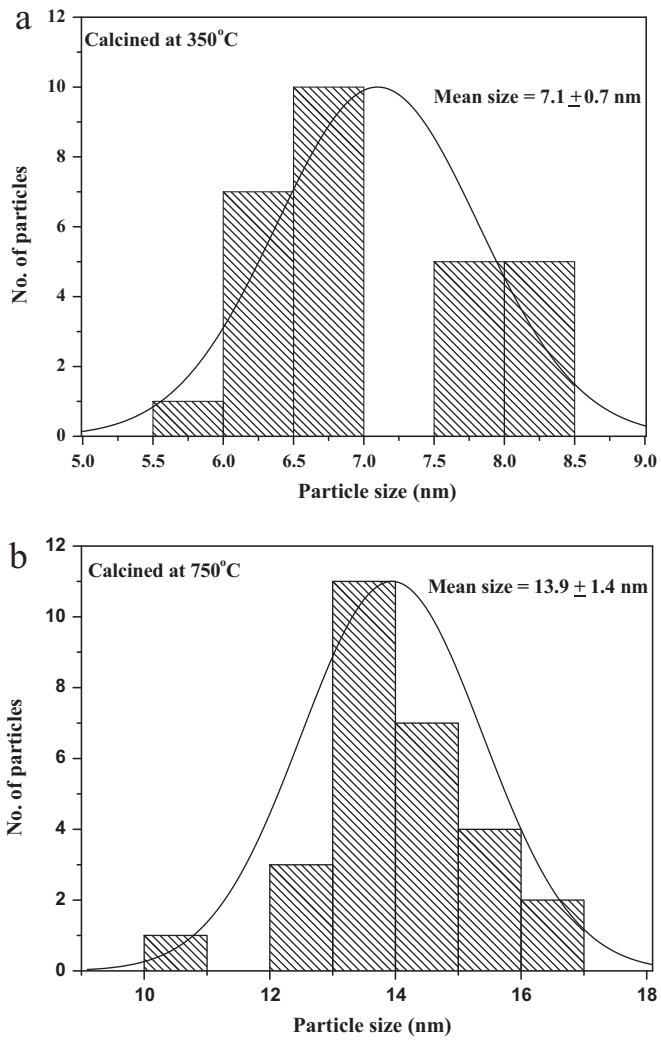

Fig. 7. Iron oxide particle size histograms of SF-1: (a) after calcination at 350 °C and (b) after calcination at 750 °C.

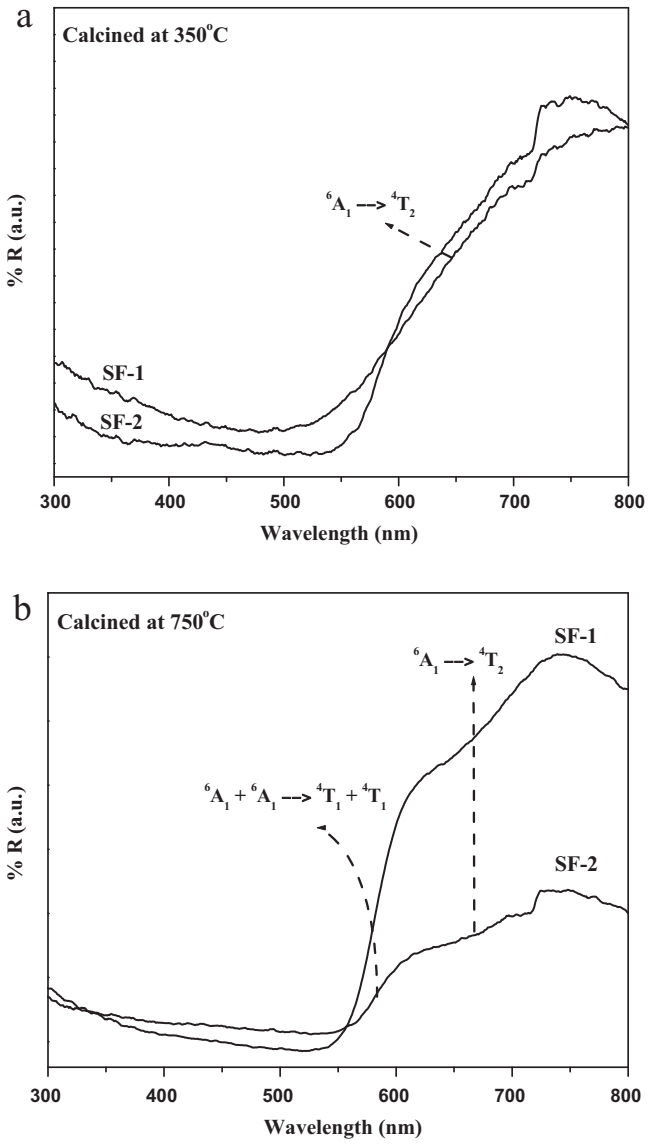

Fig. 8. Diffuse reflectance spectra of silica-iron oxide core–shell nanoparticles: (a) after calcination at 350 °C and (b) after calcination at 750 °C.

the range of 488–493 nm except for α-Fe_2O_3; for α-Fe_2O_3, the EPT appears in the range of 521–565 nm [45,46]. The electron pair transition determines the position of the absorption edge of the spectrum which in turn is related to the colour of the oxide. SF-1 and SF-2 on calcination at 350 °C show a single electron transition near 650 nm indicating the presence of iron oxide on silica. After calcination at 750 °C, the samples show single electron transition near 690 nm along with the electron pair transition near 570 nm indicating the presence of α-Fe_2O_3 on the silica spheres, in accordance with the XRD results (Fig. 1(c)).

3.7. Magnetic measurements

Magnetic measurements were carried out for the sample SF-1 which exhibits uniform deposition of iron oxide nanoparticles on silica. The magnetization versus field (M–H) plots for SF-1 before and after calcination are shown in Fig. 9. All the samples of SF-1 exhibit superparamagnetic behaviour at 300 K as well as at 5 K with negligible M_r and H_c values. Also, the iron oxide nanoparticles attain saturation magnetization at low fields (1.7–2.6 kOe) and this characteristics is important for biomedical applications [47,48]. At 300 K, the saturation magnetization (M_s) values before and after calcination at 350 °C and 750 °C are 9, 13 and 2 emu/g, respectively. The observed M_s values at 5 K for SF-1 before and after calcination at 350 °C and 750 °C are 15, 15 and 2.5 emu/g, respectively. The M_s value of the calcined SF-1 (350 °C) measured at 300 K (13 emu/g) is comparable to that of γ-Fe_2O_3/SiO_2 core–shell nanoparticles (17.2 emu/g) reported by Chen et al. [49]. Also, the M_s value is less than that of bulk γ-Fe_2O_3 (M_s = 76 emu/g at 300 K). The lower M_s value for SF-1 after calcination at 750 °C (2 emu/g) is attributed to the conversion of γ-Fe_2O_3 to α-Fe_2O_3.

SF-1 before and after calcination possess relatively higher M_s values at 5 K than at 300 K indicating ferri/ferromagnetic behaviour at 5 K where the magnetic moments are being blocked [48]. As the temperature increases, the magnetic moments become unblocked where the thermal energy exceeds the anisotropy energy barrier and interactions between magnetic moments become less [50]. The ZFC and FC curves at an applied field of 1000 Oe are shown in Fig. 10. The blocking transition is clearly seen in SF-1 after calcination at 350 °C and the T_B is 109 K. The particle volume (V) can be calculated from T_B using the following equation [51].

$$T_B = \frac{K_{eff} V}{25 k_B} \quad (2)$$

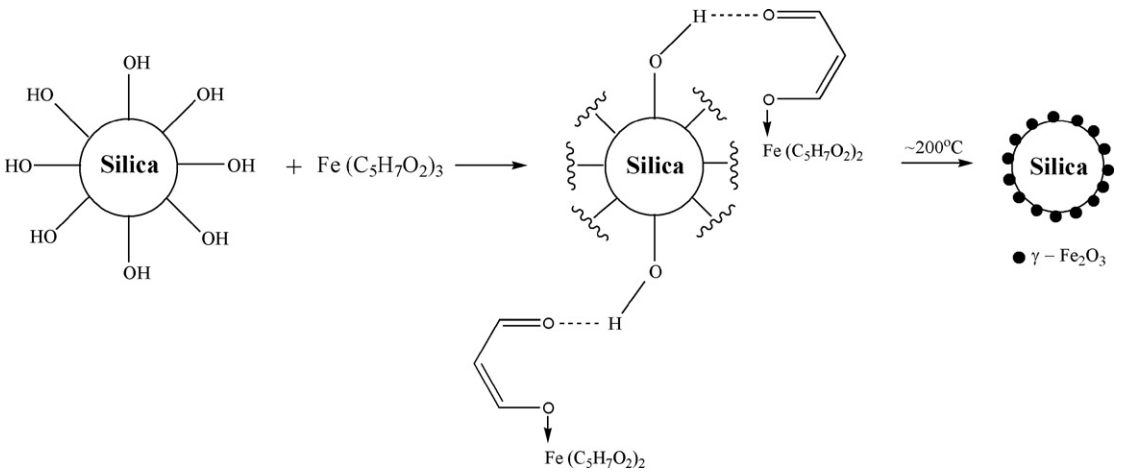

Scheme 1. Schematic representation of the anchoring of iron (III) acetylacetonate complex on the surface of silica and its further decomposition to yield iron oxide nanoparticles.

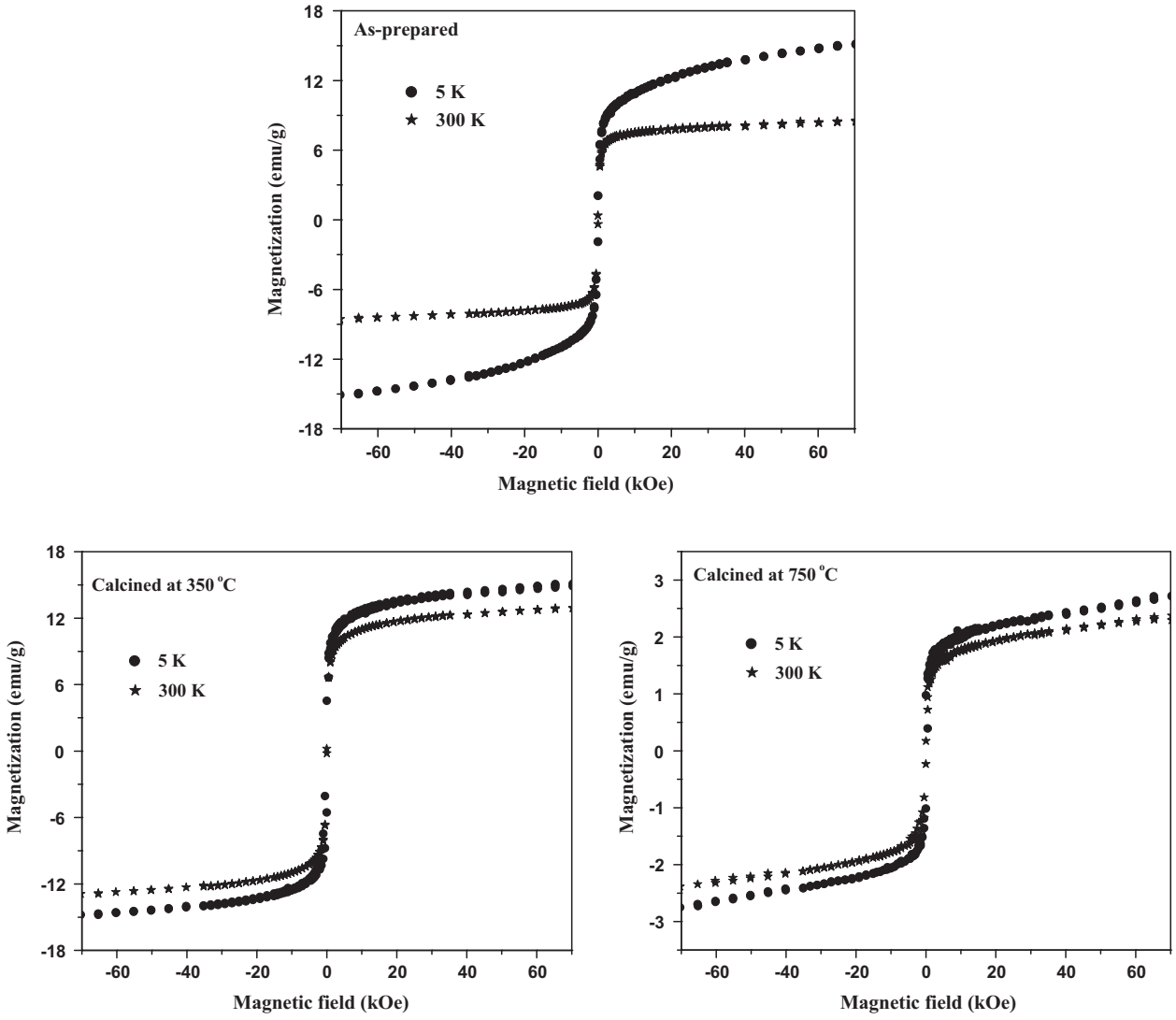

Fig. 9. *M–H* curves of the silica-iron oxide core–shell nanoparticles (SF-1) measured at 5 K and 300 K.

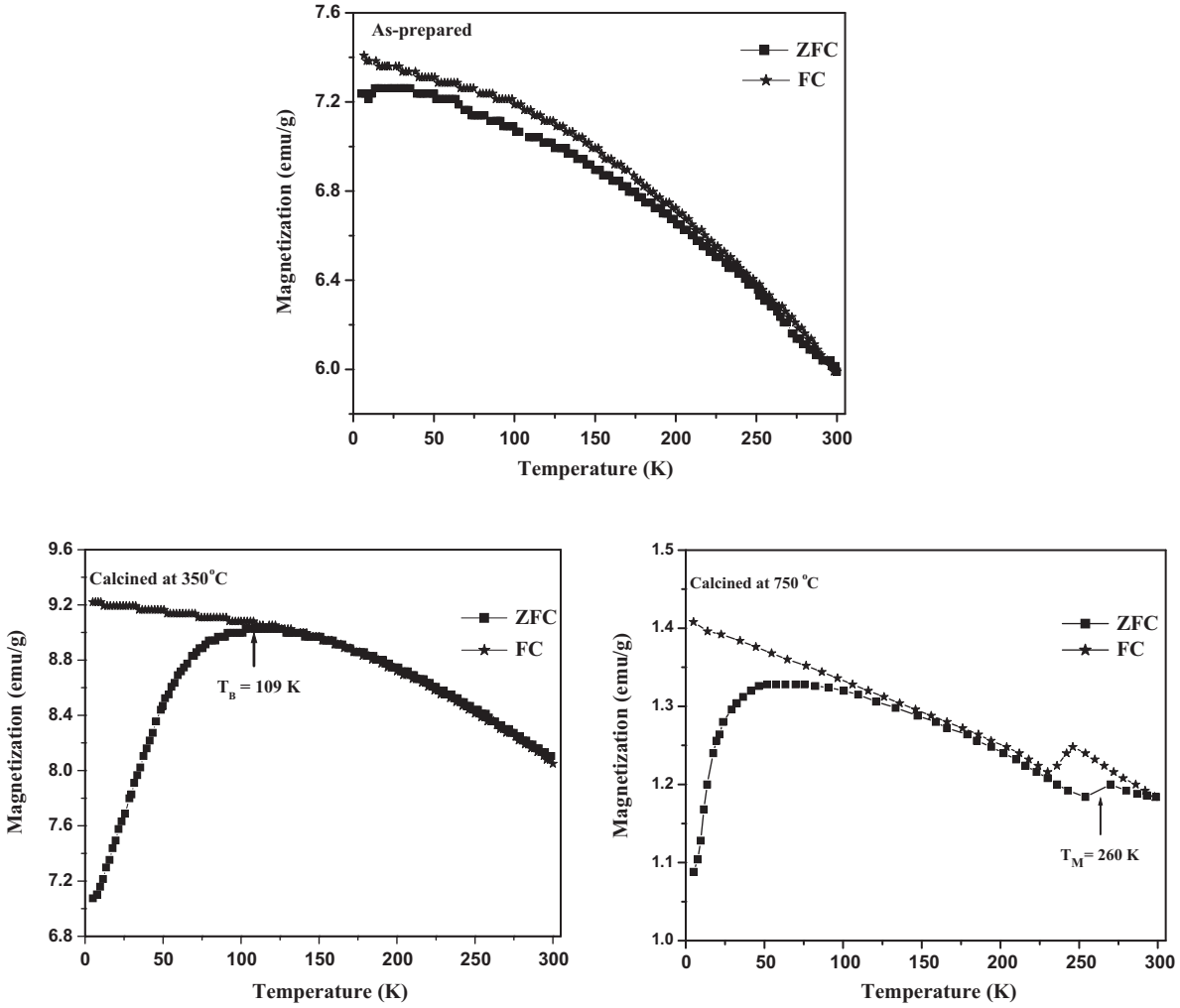

Fig. 10. ZFC and FC curves of silica-iron oxide core–shell nanoparticles (SF-1) at an applied field of 1000 Oe.

where K_{eff} is the effective anisotropy constant (for bulk maghemite, $K_{eff} = 4.7 \times 10^4$ erg cm^{-3}) and k_B is the Boltzmann's constant. The average particle size (diameter) of the iron oxide nanoparticles on silica (in SF-1 calcined at 350 °C) was calculated as 24.8 nm. It should be noted that the particle size calculated using Eq. (2) is approximate since K_{eff} can increase on reducing the particle size. The ZFC curve of SF-1 after calcination at 750 °C is broader with a blocking transition indicating a wide size distribution for the iron oxide nanoparticles. The characteristic Morin transition near 260 K is also observed in the ZFC–FC curves of SF-1 after calcination at 750 °C which indicate the presence of hematite nanoparticles on the surface of silica spheres [52].

3.8. Mechanism of formation of iron oxide nanoparticles

The interaction between iron (III) acetylacetonate and silanol groups can be explained by the H-bonding between the π-system of acetyl acetone ligand and proton of the silanol group (Scheme 1). This mode of bonding has been reported by various authors [53–55]. Anchoring of the iron complex is better in the case of activated silica, compared to unactivated silica, due to the removal of organic impurities and the removal of a few Si—OH groups that were involved in H-bonding. On activation of silica at 500 °C, the adsorbed water molecules and most of the vicinal (neighbouring) hydroxyl groups get eliminated forming siloxane (Si—O—Si) bonds; the isolated and geminal hydroxyl groups are removed only above 600 °C. It is known that the isolated and geminal hydroxyl groups are more reactive than the vicinal (neighbouring) hydroxyl groups [56]. This makes the isolated and geminal hydroxyl groups readily available for anchoring of the iron complex. A mechanistic scheme for the decomposition of iron acetylacetonate on silica has been given (Scheme 2). Iron (III) acetylacetonate thermally decomposes, in air, at about 200 °C to produce iron oxide nanoparticles (maghemite) along with by-products such as carbon monoxide, carbon dioxide, methane and water [57]. The maghemite nanoparticles are then transformed to hematite nanoparticles on the surface of silica microspheres after heat treatment at high temperatures (e.g. 750 °C), as evidenced by XRD results.

4. Photocatalytic degradation of Rhodamine B

Hematite (α-Fe_2O_3), a narrow band gap semiconductor, has been used as a catalyst for the photodegradation reactions due to its photoelectrochemical stability in aqueous solution [31,32,58–60]. Since the magnetic silica-iron oxide core–shell nanoparticles (SF-1 and SF-2) after calcination at 750 °C contain α-Fe_2O_3 nanoparticles, they were used for the photocatalytic degradation of RhB. Pure silica and iron oxide nanoparticles were also used to test their effectiveness as catalysts and a blank reaction was performed in the absence of the catalyst. The photodegradation

$$4\,(C_5H_7O_2)_3\,Fe + 17\,O_2 \xrightarrow{\sim 200^{o}C} 2\,Fe_2O_3 + 30\,CO + 10\,CO_2 + 20\,CH_4 + 2\,H_2O$$

$$\gamma - Fe_2O_3\,@\,SiO_2 \xrightarrow{> 350^{o}C} \alpha - Fe_2O_3\,@\,SiO_2$$

Scheme 2. Reaction mechanism involved in the formation of iron oxide nanoparticles by the thermal decomposition of iron (III) acetylacetonate.

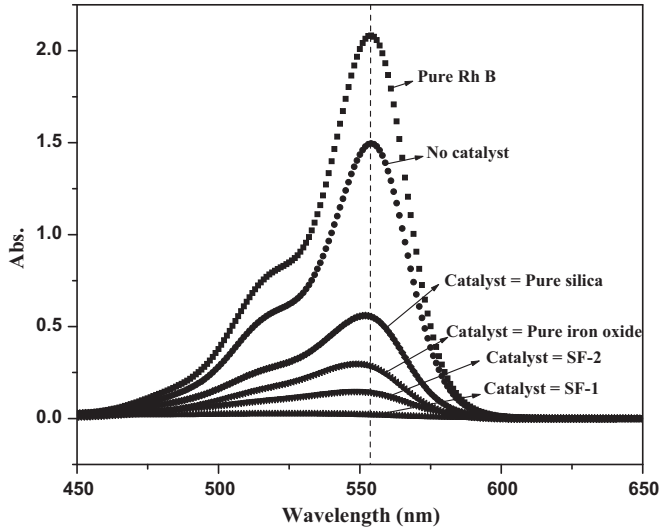

Fig. 11. Photodegradation of RhB in aqueous solution using different catalysts. The irradiation time was kept constant at 120 min.

results, as monitored by UV–visible spectroscopy, are shown in Fig. 11.

It can be noticed that the silica-iron oxide core–shell nanoparticles (SF-1 and SF-2) serve as better catalysts compared to pure silica and iron oxide nanoparticles. SF-1 calcined at 750 °C has better catalytic activity compared to SF-2 calcined at 750 °C. Kinetics of the photodegradation was carried out for the best catalyst (SF-1) (Fig. 12) and the inset in Fig. 12 shows the decrease in the concentration of RhB at λ_{max} (~555 nm) in aqueous solution with time. The complete degradation of RhB takes place in about 120 min.

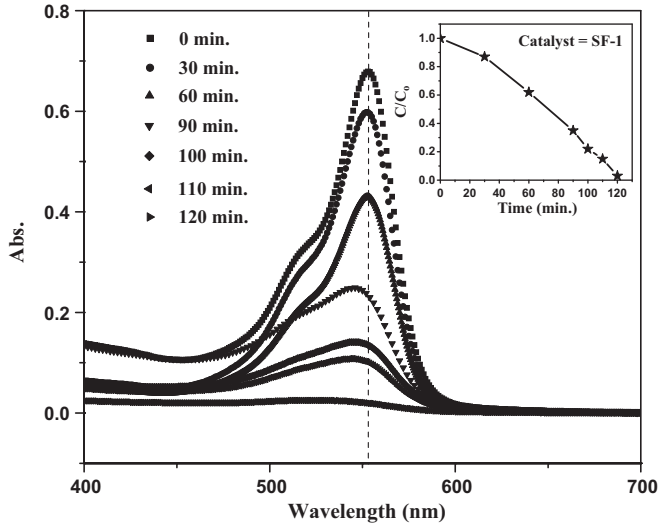

Fig. 12. Kinetics of photocatalytic degradation of RhB using SF-1 catalyst after calcination at 750 °C (The inset shows the decrease in concentration of RhB with irradiation time at λ_{max} (~555 nm). C_o is the initial concentration of the dye and C is the concentration of the dye at a given time, t.

The mechanism of degradation of RhB [32] involves the generation of charge carriers such as electrons and holes on UV light irradiation as shown in Eq. (3).

$$\alpha\text{-}Fe_2O_3 \rightarrow \alpha\text{-}Fe_2O_3(e^-, h^+) \quad (3)$$

The electrons can directly attack H_2O_2 to form hydroxyl radicals ($OH^{\bullet}$) as shown in Eq. (4).

$$H_2O_2 + e^- \rightarrow OH^- + OH^{\bullet} \quad (4)$$

Also, the electrons can be trapped by Fe^{3+} on the surface of the catalyst (Eqs. (5) and (6)).

$$Fe^{3+} + e^- \rightarrow Fe^{2+} \quad (5)$$

$$Fe^{2+} + H_2O_2 \rightarrow Fe^{3+} + OH^- + OH^{\bullet} \quad (6)$$

The hydroxyl radicals lead to the photocatalytic degradation [61] as shown in Eq. (7).

$$OH^{\bullet} + \text{Dye molecule} \rightarrow \text{intermediates}$$
$$\rightarrow CO_2\uparrow + H_2O + \text{mineral salts} \quad (7)$$

It is possible that RhB adsorbs on the surface of core–shell nanoparticles and hence there is a decrease in the absorbance in the UV–Visible spectra. But the RhB is not only adsorbed on the silica spheres but it is also degraded which can be proved as follows. With an increase in the irradiation time, the absorbance in the visible region not only decreases but also shifts to lower wavelength (Fig. 12). This has been observed by Zhou et al. indicating that both the chromophores and the aromatic rings of RhB are destroyed instead of being simply decolourized due to adsorption [32]. Based on the above studies, it is concluded that the silica-iron oxide core–shell nanoparticles are good catalysts for the photodegradation of RhB in aqueous solution.

5. Conclusions

Synthesis of silica-iron oxide core–shell nanoparticles with silica as core and iron oxide nanoparticles as shell by a simple thermal decomposition approach has been demonstrated. The iron oxide nanoparticles have been deposited uniformly on the silica spheres by this approach. The core–shell nanoparticles are superparamagnetic at room temperature and the magnetic measurements indicate the conversion of iron oxide nanoparticles from maghemite to hematite on the surface of silica microspheres on calcination at 750 °C. The silica-iron oxide core–shell nanoparticles are good catalysts for the degradation of Rhodamine B in aqueous solution. The present thermal decomposition approach may be extended for the preparation of other magnetic core–shell nanoparticles.

Acknowledgments

Generous funding from Council of Scientific and Industrial Research (Project No: 01 (2311)/09/EMR-II) is acknowledged with gratitude. Thanks are due to Institute Instrumentation Centre, IIT Roorkee for providing the XRD, FE-SEM/EDXA and SQUID facilities. Thanks are also due to Sophisticated Analytical Instruments Facility (SAIF), IIT Bombay for providing the TEM facility.

References

[1] Y. Liu, T. Xie, G. Yang, J. Mater. Sci. 46 (2011) 5050.
[2] Z. Guo, S. Bai, Y. Sun, Enzyme Microb. Technol. 32 (2003) 776.
[3] J. Wang, D. Bhattacharya, L.G. Bachas, Biomacromolecules 2 (2001) 700.
[4] E.B. Denkbas, E. Kilicay, C. Birlikseven, E. Ozturk, React. Funct. Polym. 50 (2002) 225.
[5] J. Meng, C. Shi, B. Wei, W. Yu, C. Deng, X. Zhang, J. Chromatogr. A 1218 (2011) 2841.
[6] J. Meng, J. Bu, C. Deng, X. Zhang, J. Chromatogr. A 1218 (2011) 1585.
[7] W. Jiang, Z. Sun, F. Li, K. Chen, T. Liu, J. Liu, T. Zhou, R. Guo, J. Magn. Magn. Mater. 323 (2010) 435.
[8] B. Han, N. Choi, K.H. Kim, D.W. Lim, J. Choo, J. Phys. Chem. C 115 (2011) 6290.
[9] A. Szegedi, Z. Konya, D. Mehn, E. Solymar, G. Pal-Borbely, Z.E. Horvath, L.P. Biro, I. Kiricsi, Appl. Catal. A: Gen. 272 (2004) 257.
[10] K. Bachari, J.M.M. Millet, P. Bonville, O. Cherifi, F. Figueras, J. Catal. 249 (2007) 52.
[11] M. Arruebo, M. Galan, N. Navascues, C. Tellez, C. Marquina, M.R. Ibarra, J. Santamaria, Chem. Mater. 18 (2006) 1911.
[12] T. Valdes-Solis, A.F. Rebolledo, M. Sevilla, P. Valle-Vigon, O. Bomati-Miguel, A.B. Fuertes, P. Tartaj, Chem. Mater. 21 (2009) 1806.
[13] Z. Zhang, L. Zhang, L. Chen, L. Chen, Q.H. Wan, Biotechnol. Prog. 22 (2006) 514.
[14] W. Zhao, J. Gu, L. Zhang, H. Chen, J. Shi, J. Am. Chem. Soc. 127 (2005) 8916.
[15] R. Tongpool, S. Jindasuwan, Sens. Actuators B: Chem. 106 (2005) 523.
[16] D. Barreca, W.J. Blau, G.M. Croke, F.A. Deeney, F.C. Dillon, J.D. Holmes, C. Kufazvinei, M.A. Morris, T.R. Spalding, E. Tondello, Micropor. Mesopor. Mater. 103 (2007) 142.
[17] Y. Zhu, H. Da, X. Yang, Y. Hu, Colloid Surf. A 231 (2003) 123.
[18] N. Insin, J.B. Tracy, H. Lee, J.P. Zimmer, R.M. Westervelt, M.G. Bawendi, ACS Nano 2 (2008) 197.
[19] D.K. Yi, S.T. Selvan, S.S. Lee, G.C. Papaefthymiou, D. Kundaliya, J.Y. Ying, J. Am. Chem. Soc. 127 (2005) 4990.
[20] S. Ramesh, R. Prozorov, A. Gedanken, Chem. Mater. 9 (1997) 2996.
[21] E.M. Claesson, A.P. Philipse, Langmuir 21 (2005) 9412.
[22] M. Zhang, T. Itoh, M. Abe, J. Appl. Phys. 36 (1997) 243.
[23] E. Ruiz-Hernandez, A. Lopez-Noriega, D. Arcos, I. Izquierdo-Barba, O. Terasaki, M. Vallet-Regi, Chem. Mater. 19 (2007) 3455.
[24] Z. Zhang, B.Q. Wei, P.M. Ajayan, Appl. Phys. Lett. 79 (2001) 4207.
[25] J. Kim, J.E. Lee, J. Lee, J.H. Yu, B.C. Kim, K. An, Y. Hwang, C.H. Shin, J.G. Park, J. Kim, T. Hyeon, J. Am. Chem. Soc. 128 (2006) 688.
[26] M. Asada, Y. Hara, Y. Kuroda, S. Tanaka, T. Horikawa, Y. Miyake, Ind. Eng. Chem. Res. 48 (2009) 2577.
[27] L. Ding, W. Zhou, H. Chu, Z. Jin, Y. Zhang, Y. Li, Chem. Mater. 18 (2006) 4109.
[28] J.Q. Lu, N. Moll, Q. Fu, J. Liu, Chem. Mater. 17 (2005) 2237.
[29] L. Li, E.S.G. Choo, X. Tang, J. Ding, J. Xue, Chem. Commun. (2009) 938.
[30] S. Abramson, C. Meiller, P. Beaunier, V. Dupuis, L. Perrigaud, A. Bee, V. Cabuil, J. Mater. Chem. 20 (2010) 4916–4924.
[31] S. Bharathi, D. Natraj, D. Mangalraj, Y. Masuda, K. Senthil, K. Yong, J. Phys. D: Appl. Phys. 43 (2010) 015501/1.
[32] X. Zhou, H. Yang, C. Wang, X. Mao, Y. Wang, Y. Yang, G. Liu, J. Phys. Chem. C 114 (2010) 17051.
[33] A. Mehrdad, B. Massoumi, R. Hashemzadeh, Chem. Eng. J. 168 (2011) 1073.
[34] D. Yu, R. Cai, Z. Liu, Spectrochim. Acta A 60 (2004) 1617.
[35] W. Stöber, A. Fink, E. Bohn, J. Colloids Interface Sci. 26 (1968) 62.
[36] V.G. Pol, A. Gedanken, J. Calderon-Moreno, Chem. Mater. 15 (2003) 1111.
[37] F. Unoba, B. Wongsiri, N. Phaeon, M. Puanngam, J. Shiowatana, J. Hazard. Mater. 142 (2007) 455.
[38] S. Dixit, P. Jeevanandam, Adv. Mater. Res. 67 (2009) 221.
[39] T. Tuval, A. Gedanken, Nanotechnology 18 (2007) 255601/1.
[40] F. Tielens, C. Gervais, J.F. Lambert, F. Mauri, D. Costa, Chem. Mater. 20 (2008) 3336.
[41] S. Bruni, F. Cariati, M. Casu, A. Lai, A. Musinu, G. Piccaluga, S. Solinas, Nanostruct. Mater. 11 (1999) 573.
[42] F. Rubio, J. Rubio, J.L. Oteo, Spectrosc. Lett. 31 (1998) 199.
[43] K.C. Baric, B.S.D. Ch, S. Varaprasad, D. Bahadur, J. Non-Cryst. Solids 356 (2010) 153.
[44] D. Li, W.Y. Teoh, C. Selomulya, R.C. Woodward, P. Munroe, R. Amal, J. Mater. Chem. 17 (2007) 4876.
[45] R.M. Cornell, U. Schwertmann, The Iron Oxides, Structure, Properties, Reactions, Occurrences and Uses, 2nd ed., Wiley-VCH, 2003.
[46] A.C. Scheinost, A. Chavernas, V. Barron, J. Torrent, Clay Clay Miner. 46 (1998) 528.
[47] B. Chen, W. Wu, X. Wang, Curr. Cancer Drug Tar. 11 (2011) 184.
[48] M. Mahmoudi, A. Simchi, M. Imani, J. Iran. Chem. Soc. 7 (2010) S1.
[49] F. Chen, R. Shi, Y. Xue, L. Chen, Q.H. Wan, J. Magn. Magn. Mater. 322 (2010) 2439.
[50] G.G. Couto, J.J. Klein, W.H. Schreiner, D.H. Moska, A.J.A. de Oliveira, A.J.G. Zarbin, J. Colloid Interface Sci. 311 (2007) 461.
[51] E.C. Stoner, E.P. Wohlfarth, Trans. Roy. Soc. A 240 (1948) 599.
[52] S. Liu, J. Zhou, L. Zhang, J. Phys. Chem. C 115 (2011) 3602.
[53] P. Kustrowski, L. Chmielarz, R. Dziembaj, P. Cool, E.F. Vasant, J. Phys. Chem. B 109 (2005) 11552.
[54] M.C. Brasil, E.V. Benvenutti, J.R. Gregorio, A.E. Gerbase, React. Funct. Polym. 63 (2005) 135.
[55] V. Matsura, Y. Guari, J. Larionova, C. Guerin, A. Caneschi, C. Sangregorio, E. Lancelle-Beltran, A. Mehdi, R.J.P. Corriu, J. Mater. Chem. 14 (2004) 3026.
[56] O. Sneh, S.M. George, J. Phys. Chem. 99 (1995) 4639.
[57] A.C. Rastogi, S. Dhara, B.K. Das, J. Electrochem. Soc. 142 (1995) 3148.
[58] H. Zhou, S.S. Wong, ACS Nano 2 (2008) 944.
[59] Y. Wang, W. Du, Y. Xu, Langmuir 25 (2009) 2895.
[60] Q. Wei, Z. Zhang, Z. Li, Q. Zhou, Y. Zhu, J. Phys. D: Appl. Phys. 41 (2008) 202002/1.
[61] K. Byrappa, A.K. Subramani, S. Ananda, K.M.L. Rai, R. Dinesh, M. Yoshimura, Bull. Mater. Sci. 29 (2006) 433.